



Contents lists available at ScienceDirect

## Arabian Journal of Chemistry

journal homepage: [www.ksu.edu.sa](http://www.ksu.edu.sa)

Original article



# Iron borophosphate glasses: Merging optical transparency, structural integrity, and radiation shielding efficacy for sustainable uses

Kholood Alkhamis<sup>a</sup>, Hawra A. Alghasham<sup>b</sup>, Albandary Almahri<sup>c</sup>, Hussain Alessa<sup>d</sup>, Oumr Adnan Osra<sup>e</sup>, S.A. Al-Ghamdi<sup>f</sup>, Adel M. Binyaseen<sup>e</sup>, Nashwa M. El-Metwaly<sup>d,g,\*</sup>

<sup>a</sup> Department of Chemistry, College of Science, University of Tabuk, 71474 Tabuk, Saudi Arabia

<sup>b</sup> Department of Physics, Faculty of Sciences, Umm Al-Qura University, Makkah, Saudi Arabia

<sup>c</sup> Department of Chemistry, College of Science and Humanities in Al-Kharj, Prince Sattam Bin Abdulaziz University, Al-Kharj 11942, Saudi Arabia

<sup>d</sup> Department of Chemistry, Faculty of Science, Umm Al-Qura University, Makkah 24230, Saudi Arabia

<sup>e</sup> Department of Architecture, Faculty of Engineering and Architecture, Umm Al-Qura University, Makkah 24381, Saudi Arabia

<sup>f</sup> Department of Physics, College of Science, University of Tabuk, 71474 Tabuk, Saudi Arabia

<sup>g</sup> Department of Chemistry, Faculty of Science, Mansoura University, EL-Gomhoria Street 35516, Egypt

## ARTICLE INFO

## Keywords:

Borophosphate glass

Iron oxide

UV/Vis. Spectra

DAT

Radiation shielding

## ABSTRACT

The research work explored the influence of iron doping on the optical behavior, structural characteristics, and radiation shielding capabilities of soda lime borophosphate glass system of composition  $x\text{Fe}_2\text{O}_3-(42.5-x)\text{B}_2\text{O}_3-26\text{CaO}-28.7\text{Na}_2\text{O}-2.8\text{P}_2\text{O}_5$  ( $x$  up to 8 mol%). The glass samples doped with varying iron concentrations were synthesized via the conventional melt-quenching method. A comprehensive characterization approach was employed, integrating X-ray diffraction (XRD) analysis to probe the structural aspects, Fourier transform infrared (FTIR) spectroscopy to examine the molecular vibrations and bonding, and UV-visible spectroscopic techniques to investigate the optical properties. Furthermore, the study evaluated the potential of these iron-doped glasses as effective radiation shielding materials by assessing their attenuation performance against various radiation types. The influence of iron oxide ( $\text{Fe}_2\text{O}_3$ ) addition on the borophosphate network, coordination environment, and optical absorption was examined. The radiation shielding characteristics, such as mass attenuation coefficient, half-value layer, mean free path, and other parameters, were assessed using Phy-x freeware program calculations. The results revealed the formation of an amorphous glass structure and the incorporation of iron ions into the borophosphate network. The addition of  $\text{Fe}_2\text{O}_3$  influenced the borate superstructural units, the conversion of  $\text{BO}_3$  to  $\text{BO}_4$  units, and the optical absorption bands. The glasses exhibited promising radiation shielding properties combined with increasing  $\text{Fe}_2\text{O}_3$  content.

## 1. Introduction

Borophosphate glasses represent an important class of multi-component vitreous materials formed primarily by various combinations of  $\text{B}_2\text{O}_3$  and  $\text{P}_2\text{O}_5$  glass-former oxides along with network modifying components like alkali/alkaline earth oxides. The intrinsic properties of the constituent oxides allow for tunable structural modifications and tailored chemical/physical characteristics in borophosphate glass systems through appropriate compositional design (Carta et al., 2008; Kim et al., 2010; Abdelghany et al., 2024). The borate glass network comprises planar  $\text{BO}_3$  triangles connected by bridging oxygen atoms in a wide variety of borate superstructural units,

depending on the  $\text{B}_2\text{O}_3$  concentration. Common structural groups include diborate, triborate, pentaborate, and higher-order units linked via B-O-B bonds. The introduction of  $\text{P}_2\text{O}_5$  leads to the formation of long metaphosphate chains (Q2 tetrahedra) along with rings (Q1 diphosphate units) based on P-O-P connections (Griscom, 1978; Brow, 2000). The relative fractions of various borate superstructural groups and phosphate units may be controlled by the  $\text{B}_2\text{O}_3/\text{P}_2\text{O}_5$  ratio which significantly influences the optical, thermal, physical, and structural attributes. The addition of alkali and alkaline earth oxides promotes the breakdown of B-O-B and P-O-P bonds allowing a greater number of non-bridging oxygen atoms, thereby enabling the engineering of glass properties as per specific requirements (Freudenberger, 2023).

\* Corresponding author at: Department of Chemistry, Faculty of Science, Umm Al-Qura University, Makkah 24230, Saudi Arabia.

E-mail addresses: [nmmohamed@uqu.edu.sa](mailto:nmmohamed@uqu.edu.sa), [n\\_elmetwaly00@yahoo.com](mailto:n_elmetwaly00@yahoo.com) (N.M. El-Metwaly).

<https://doi.org/10.1016/j.arabjc.2024.105875>

Received 9 April 2024; Accepted 12 June 2024

Available online 17 June 2024

1878-5352/© 2024 The Author(s). Published by Elsevier B.V. on behalf of King Saud University. This is an open access article under the CC BY-NC-ND license (<http://creativecommons.org/licenses/by-nc-nd/4.0/>).

Sodium calcium borophosphate belongs to an important subclass of borophosphate glasses where  $\text{Na}_2\text{O}$  and  $\text{CaO}$  components serve as intermediate/modifier oxides. The assimilation of  $\text{Na}^+$  ions expands the borate glass networks via the creation of non-bridging oxygen leading to the formation of  $[\text{BO}_4]$  units. The larger  $\text{Ca}^{2+}$  ions demonstrate preferential affinity towards phosphate anions, transforming longer metaphosphate chains into shorter pyro- and orthophosphate units enriched with terminal P-O bonds (Youssef et al., 2000). The collaborative interactions between  $\text{Na}^+$ ,  $\text{Ca}^{2+}$ ,  $\text{B}^{3+}$ , and  $\text{P}^{5+}$  species in the quenched vitreous state enable excellent thermal and mechanical stability along with high transparency, low phonon energy, good rare-earth ion solubility, and ease of fabrication into glass-ceramics (Abdelghany et al., 2016). Soda lime borophosphate glasses thus offer suitable hosts for developing materials systems with specialized optical and dielectric applications (Brauer and Möncke, 2016).

Various transition metal oxides (TMOs) and rare-earth (RE) ion dopants have been extensively incorporated into inorganic glass matrices owing to their intriguing optical, electronic, magnetic, and spectroscopic properties originating from the unfilled d- or f- inner shell electron configurations (Sadeq and Abdo, 2021). Depending on charge-radius ratio considerations, transition metal oxides can act as intermediates or function in network modifying roles. Assimilation is an integral part of the host amorphous matrix, the transition metal ions can impart characteristic optical absorption bands, modified electronic configuration, and intrinsic spectroscopic signatures (Al-Baradi et al., 2022). Among different transition metal oxide dopants, iron oxide is commonly added to glass compositions and can exist both as isolated entities or clusters within distorted coordination fields in the glassy state. The unpaired d-shell electrons give rise to intrinsic optical transitions and paramagnetic resonance signals which serve to characterize local structural order around iron sites (Osipova et al., 2019). The three advantages of developed iron borophosphate glasses, i.e. transparency, strength, and radiation shielding make them appropriate for a wide range of applications. As glass has multi-diverse uses in environments including buildings, furniture, accessories, and appliances, iron borophosphate glasses would be a suitable material for designers. Glass curtain walls in giant buildings and skyscrapers should possess a high level of transparency, strength, and radiation protection, and that is what this developed glass fosters. In buildings, architects are concerned about glass transparency and clarity to interact with external views. Engineers usually place a strong emphasis on the strength and stability of glass to overcome the threat of wind force. Furthermore, in high-rise buildings, radiation protection becomes a critical issue. However, measures concerned with minimizing heat transfer using insulation techniques and types of materials must be balanced with maintaining adequate optical transparency for architectural and aesthetic considerations. The developed glass in this research aims to achieve an optimum balance between radiation shielding capability and optical transparency for potential applications in building envelopes.

The presence of high atomic number and density elements like Fe, Ca, and Na increases the probability of radiation attenuation through combined photoelectric absorption and Compton scattering events (Mansouri et al., 2020). This enables effective shielding against harmful gamma rays and neutron fluxes with dimensional stability and adequate mechanical strength. Borophosphate glasses with multi-component oxide additions can offer economically feasible substitutes to lead-based radiation shielding systems with sufficient transparency for vision panel applications in the nuclear industry (Khattari et al., 2024). The soda lime borophosphate glass system modified with iron oxide dopant offers immense application potential owing to the combined attributes inherited from the constituent components which may be tuned as per requirements.

By investigating the influence of iron doping on the soda-lime borophosphate glass system, the study aimed to explore the potential for enhancing radiation shielding capabilities while also gaining insights into the structural and optical property modifications induced by iron

ions in this specific glass composition.

## 2. Experimental work

### 2.1. Materials and glass preparation

Analytical grade chemicals of orthoboric acid ( $\text{H}_3\text{BO}_3$ ) as a source for boron oxide ( $\text{B}_2\text{O}_3$ ) supplied by Lab. Rasayan, Ammonium dihydrogen orthophosphate  $\text{NH}_4\text{H}_2\text{PO}_4$  as a source for phosphorus pentoxide ( $\text{P}_2\text{O}_5$ ) supplied by Sigma Aldrich Co. Sodium oxide and calcium oxide were drawn from their carbonate partner supplied by Lenxns Co. Iron oxide ( $\text{Fe}_2\text{O}_3$ ) was supplied by Sigma Aldrich and used as received. Prepared composition simulates modified Hench bioglass 45S5 containing (45 $\text{B}_2\text{O}_3$ -24.5 $\text{CaO}$ -24.5 $\text{Na}_2\text{O}$ -6 $\text{P}_2\text{O}_5$  wt% with full replacement of silicon oxide with boron oxide). The composition equivalent to (42.5 $\text{B}_2\text{O}_3$ -26 $\text{CaO}$ -28.7 $\text{Na}_2\text{O}$ -2.8 $\text{P}_2\text{O}_5$  mol%).

Accurately weighted chemicals were mixed in an agate mortar and transferred into a porcelain crucible placed in an oven adjusted at 400 °C for 2 h to ensure the removal of water, carbon dioxide, and ammonia. The temperature was then raised to about 1150–1200 °C for another 2 h. The melt was swirled occasionally many times to ensure homogeneity and bubble-free samples. The melt was then poured into a heated stainless-steel mold of the required dimensions and transferred to an oven adjusted at 350 °C. The oven was switched off and kept cooling gradually to room temperature. Samples were then transferred to a dry place until use. Sample abbreviation along with composition was shown in Table 1 while the change in color with the addition of iron oxide was observed in Fig. 1.

### 2.2. Sample characterization and radiation shielding calculations

X-ray diffraction patterns (XRD) were recorded for pulverized samples using a BRUKER D8 adopting Cu target operating at 40 kV-40 mA with ( $\lambda = 1.54 \text{ \AA}$ ). FTIR vibrational spectra recorded via a double beam Nicolet is 10 spectrometer using KBr disc route within the wavenumber range extended between 2000–400  $\text{cm}^{-1}$ . Optical absorption spectral data were measured for polished glass samples using (UV-vis) spectrophotometer (V-750) within the range from 190-1100 nm. The sample density ( $\rho_s$ ) of the glass samples was calculated using Archimedes' method utilizing xylene as an immersion solvent at room temperature.

The radiation shielding characteristics were estimated using online calculations via Phys-x software within a photon energy range between 15 keV to 15 MeV.

## 3. Results and discussion

### 3.1. X-ray diffraction

X-ray diffraction is an important tool that describes periodic or non-periodic structures of the studied sample and can be considered as a fingerprint that approves the formation of specific crystalline phases within the structure (Lepry and Nazhat, 2020). Fig. 2 reveals the XRD pattern of the studied soda lime borophosphate glass containing variable amounts of iron oxide. Amorphous borate glasses lack long-range structural periodicity and do not show crystalline Bragg peaks in the

**Table 1**  
Composition and abbreviations of the studied glasses.

Sample	CaO mol%	Na <sub>2</sub> O	B <sub>2</sub> O <sub>3</sub>	P <sub>2</sub> O <sub>5</sub>	Fe <sub>2</sub> O <sub>3</sub>
S1	26	28.7	42.5	2.8	0
S2	26	28.7	41.5	2.8	1
S3	26	28.7	40.5	2.8	2
S4	26	28.7	38.5	2.8	4
S5	26	28.7	34.5	2.8	8

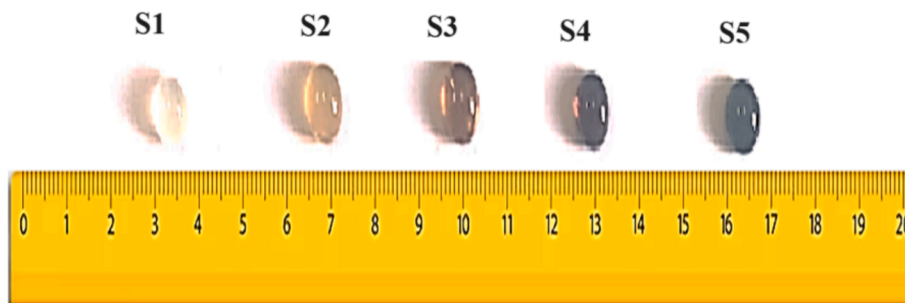


Fig. 1. change in glass color with the addition of iron oxide.

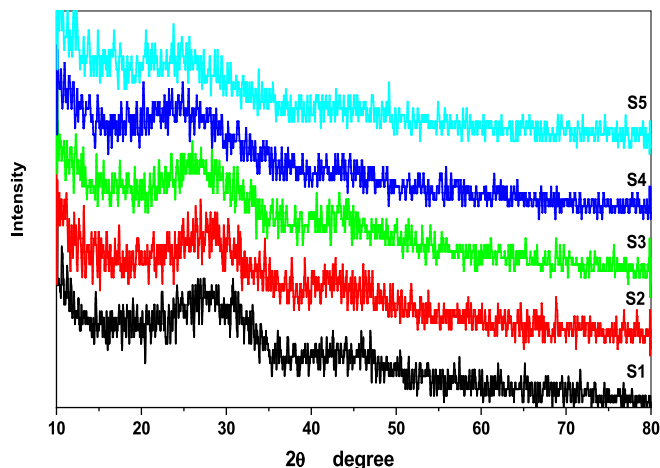


Fig. 2. XRD pattern of studied glasses.

XRD pattern Instead, a very broad diffraction halo is observed, indicating short-range disorder in the atomic structure and absence of grain boundaries. This amorphous halo is centered around  $2\theta$  values of  $10^\circ$  to  $35^\circ$ , depending on the exact glass composition.

Several authors (Lepry and Nazhat, 2020; Heuser and Nofz, 2022; Ohtori et al., 2001; Heuser et al., 2022) describe the broad peak maximum occurring near  $18^\circ$  in the case of alkali borate glasses, while for alkaline earth-containing borates, it shifts closer to  $25^\circ$ . Peak position also shifts to higher angles with increasing boron content, as  $\text{BO}_3$  units dominate over  $\text{BO}_4$  units leading to more tightly packed structural formations. The width and intensity of the amorphous halo provide information about deviation from periodicity and extent of disorder in the borate glass structure. Increased peak widths also suggest enhanced glass-forming ability and resistance against crystallization on heating.

### 3.2. FTIR optical absorption spectra

Infrared spectroscopy serves as an invaluable tool to probe the short-range structural variations in glass networks based on characteristic vibrational modes of the coordination complexes. However, unraveling individual bond signatures from the complex IR spectral profile poses considerable challenges owing to extensive peak overlaps (Kamitsos, 2015). Advanced computational techniques like derivative spectroscopy and curve-fitting methods help resolve the convoluted spectral features into constituent bands. Such bands represent specific structural groups coordinated with iron species based on changes in relative peak intensities and slight band shifts (Gautam et al., 2012, 2012).

Iron represents a conditional intermediate glass component, capable of adopting both trivalent  $\text{Fe}^{3+}$  or divalent  $\text{Fe}^{2+}$  oxidation states. However, according to the charge balance considerations, the stable trivalent form is the most favored in oxide glass hosts (Dyar, 1985). In the  $\text{Fe}^{3+}$  state, it coordinates with non-bridging oxygen atoms from the borate/

phosphate network forming distorted  $[\text{FeO}_4]$  trigonal bipyramidal or  $[\text{FeO}_6]$  octahedral units as the predominant typical coordination (Dunaeva et al., 2012). Each of these polyhedral structures exhibits characteristic vibrational modes discernible using FTIR spectroscopy.

At higher loadings beyond solubility limits, clustered formations of  $\text{Fe}^{3+}$  ions may occur which also possess identifiable spectral markers (Donald et al., 2006). The presence of minor  $\text{Fe}^{2+}$  fractions owing to a partial reduction of  $\text{Fe}^{3+}$  cannot be discounted. These effectively serve as network modifiers contributing free electrons and influencing optical properties (Romero-Perez et al., 2001). Fourier transforms infrared absorption spectra of an iron oxide containing soda lime borophosphate glasses comprised of multiple overlapping peaks representing various  $[\text{BO}_3]$ ,  $[\text{BO}_4]$ ,  $[\text{PO}_4]$ ,  $[\text{FeO}_4]$ , and  $[\text{FeO}_6]$  structural groups along with other impurities (Brauer and Möncke, 2016).

Derivative spectroscopy aids the identification of precise band positions and relative amplitudes. Curve-fitting procedures facilitate reliable separation into Gaussian components centered around specific wave-number regimes indicative of coordination fields (Sadeq and Abdo, 2021). The frequencies and full-width-at-half-maxima provide information regarding bond strengths and structural order/disorder phenomena respectively. The peak area percentages determine the relative abundances of various groups, allowing quantitative assessment of changing network configurations with progressive iron assimilation (Al-Baradi et al., 2022; Kamitsos, 2015).

Fig. 3(a) displays the FTIR spectra in the  $2000\text{--}400\text{ cm}^{-1}$  range for soda lime borophosphate glasses with 0–10 mol%  $\text{Fe}_2\text{O}_3$  addition prepared by standard melt-quench technique. A broad absorption regime is observed spanning across the mid-IR region comprising several overlapping peaks representing various structural groups.

The first-order derivative profile highlights precise inflection points more clearly as depicted in Fig. 3(b). The negative bands accurately

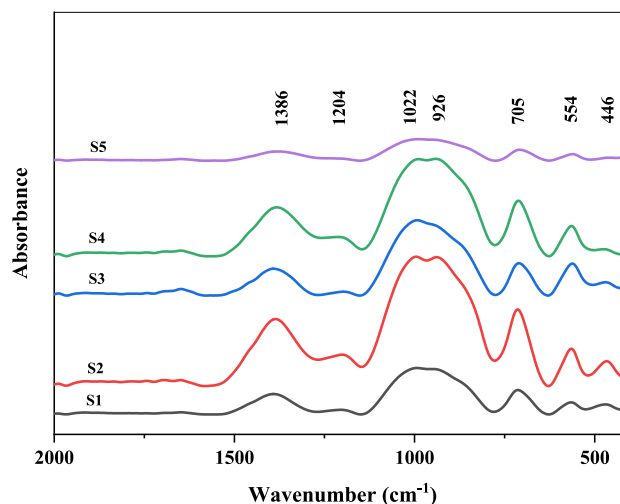


Fig. 3a. FTIR spectral data of studied glasses.

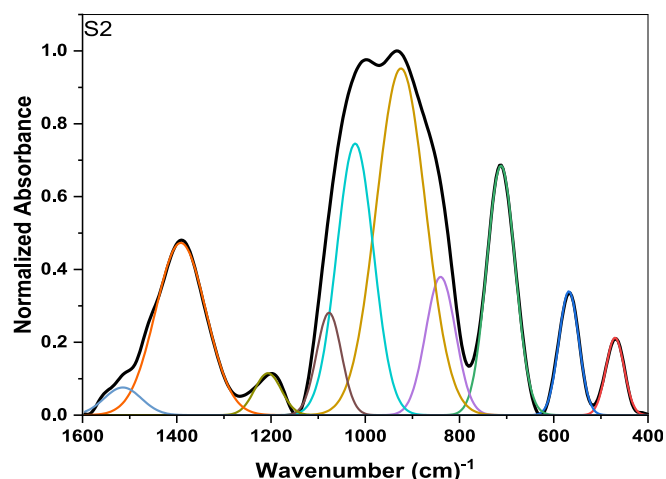


Fig. 3b. Deconvolution data of sample containing 1 mol% iron oxide.

indicate true peak positions devoid of shifts arising from shoulders/tails. Prominent minima are revealed centered around 705, 926, 1022, 1204, and 1386  $\text{cm}^{-1}$  wavenumbers.

The original FTIR spectra are curve-fitted using these derivative minima as initial centroid positions for the Gaussian peaks. The IR bands are accordingly resolved into eight constituent structural components as shown in Fig. 3. The independence of FTIR peak frequencies on composition aids the universal application of reference peak positions across the glass series during curve-fitting procedures. Only relative intensities may vary following changing structural configurations (Kamitsos, 2003; Abdelghany, 2010).

The deconvoluted spectrum fitting composition-invariant Gaussian peaks enable reliable quantitative examination of evolving structural units with iron oxide additions in soda-lime borophosphate glasses. Fig. 3(b) reveals an example of the sample containing 1 mol% iron oxide. The specific positions and intensities of these deconvoluted bands can provide insights into the structural arrangements, connectivity, and relative concentrations of different borate groups within the glass network.

N4 is specifically defined as the ratio of tetrahedral  $\text{BO}_4$  units to the sum of tetrahedral  $\text{BO}_4$  and trigonal  $\text{BO}_3$  units in borate glass compositions and their value is controlled through the effect of network modifiers on the conversion of  $\text{BO}_3$  units to  $\text{BO}_4$  units. The addition of network modifiers (such as  $\text{Na}_2\text{O}$  and  $\text{CaO}$  in this case) promotes the conversion of  $\text{BO}_3$  units to  $\text{BO}_4$  units, increasing the N4 value. However, the exact relationship between the composition and the N4 value is complex and depends on various factors, such as the relative amounts of network formers and modifiers, the presence of other structural units (e.g.,  $\text{P}_2\text{O}_5$ ), and the melting conditions. Based on the relatively high content of network modifiers ( $28.7\text{Na}_2\text{O} + 26\text{CaO} = 54.7 \text{ mol}\%$ ), we can expect a higher N4 value, possibly in the range of 0.4 to 0.7. such ratio can be calculated using the deconvoluted FTIR data through calculations adopting obtained relative areas for such function groups as reported by several authors (Elbasuoni et al., 2024; Abdelghany et al., 2017; Yianopoulos et al., 2001; Topper et al., 2023). A reasonable value for the N4 value in base soda lime borophosphate glass composition was found to be around 0.5, indicating that approximately half of the borate units are present as  $\text{BO}_4$  tetrahedral units, and the other half as  $\text{BO}_3$  trigonal units.

When iron oxide ( $\text{Fe}_2\text{O}_3$ ) replaces the same amount of the  $\text{B}_2\text{O}_3$  in the given borate glass composition, it can potentially affect the glass structure and properties through the following (Abou Hussein and Barakat, 2022; Abou Hussein and Abdel-Galil, 2023; Abou Hussein et al., 2021):

- Network former/modifier balance: In glass structures, network formers (e.g.,  $\text{B}_2\text{O}_3$ ,  $\text{P}_2\text{O}_5$ ) create the glass network, while network

modifiers (e.g.,  $\text{Na}_2\text{O}$ ,  $\text{CaO}$ ) modify the network by creating non-bridging oxygens. Replacing  $\text{B}_2\text{O}_3$  with  $\text{Fe}_2\text{O}_3$  can affect this balance.

- Depending on its coordination environment within the glass structure,  $\text{Fe}_2\text{O}_3$  can act as a network former or modifier. If it acts as a network former, it can further depolymerize (break up) the borate network, potentially increasing the N4 value (proportion of tetrahedral borate units).
- Iron can exist in two oxidation states,  $\text{Fe}^{2+}$  and  $\text{Fe}^{3+}$ , in glasses. The presence of both these ions can create a mixed ionic-covalent character in the glass network, affecting its physical and optical properties.
- If  $\text{Fe}_2\text{O}_3$  acts as a network former, it can further break up the borate network by creating more non-bridging oxygens, potentially increasing the proportion of tetrahedral borate units (N4 value).
- The changes in the glass network structure, the mixed ionic-covalent character due to  $\text{Fe}^{2+}$  and  $\text{Fe}^{3+}$ , and the potential increase in N4 value can influence various physical and optical properties of the glass, such as density, thermal stability, refractive index, and optical absorption/transmission.

Calculation of the N4 value for such composition may shed light on the role of iron oxide and possible changes in the properties of the studied glasses. The calculated N4 value was estimated as shown in Table 2. The decrease in the value when iron reaches 8 mol% suggests the presence of iron in both former and modifier sites within the glass structure.

### 3.3. UV/Vis optical absorption spectra

Fig. 4 reveals UV/Vis. spectral data of the prepared samples. The UV-visible spectra of borate glasses often show characteristic absorption bands that provide insights into the glass structure and the effects of adding transition metal ions like iron. The peak at about 240 nm may be attributed to electronic transitions in the  $\text{BO}_3$  structural units of the borate glass network corresponding to  $\pi\text{-}\pi^*$  transitions of O-B-O linkages indicating the presence of trigonal  $\text{BO}_3$  units as the main borate species (Marzouk and Elbatal, 2014). Several authors attributed such peaks to the presence of iron as a contamination in the chemicals used for the preparation of glasses even at ppm level (Marzouk et al., 2017; Shashikala and Udayashankar, 2020). The shoulder at  $\sim 305$  nm is considered to be related to charge transfer transitions in  $\text{Fe}^{3+}$  ions representing ligand-metal ( $\text{O}_2\text{-Fe}^{3+}$ ) charge transfer reported by several authors (Ehrt and Möncke, 2002; Volotinen and Pehlivan, 2022).

The band at  $\sim 375$  nm considered to be arising from d-d transitions in  $\text{Fe}^{3+}$  ions specifically corresponds to  ${}^6\text{A}_{1g} \rightarrow {}^4\text{T}_{1g}$  (G) transitions and indicates the presence of  $\text{Fe}^{3+}$  ions occupying tetrahedral sites still increased and red-shifted, but when the Fe concentration becomes 8 % it showed a broad band.

The UV-vis spectra provide characteristic fingerprints regarding the  $\text{B}^{3+}$  coordination state and the incorporation of  $\text{Fe}^{3+}$  ions in interstitial sites in the borate glass structure. The growth of 305 and 375 nm peaks indicates the progressive inclusion of  $\text{Fe}^{3+}$  ions in the glass network with additional iron oxide content.

Calculating the direct and indirect optical energy bandgap ( $E_g$ ) of glasses provides an understanding of the electronic structure and availability of electronic transitions. A lower indirect gap suggests transitions through band tails needing phonon assistance. Larger bandgaps allow a wider wavelength transparency range. Glasses with bandgaps  $> 3$  eV can enable good visible light transmission. In addition, it can help predict some electrical properties. Smaller bandgaps

Table 2  
estimated values of N4 for the studied glasses.

Sample	S1	S2	S3	S4	S5
N4	0.52	0.53	0.54	0.59	0.55

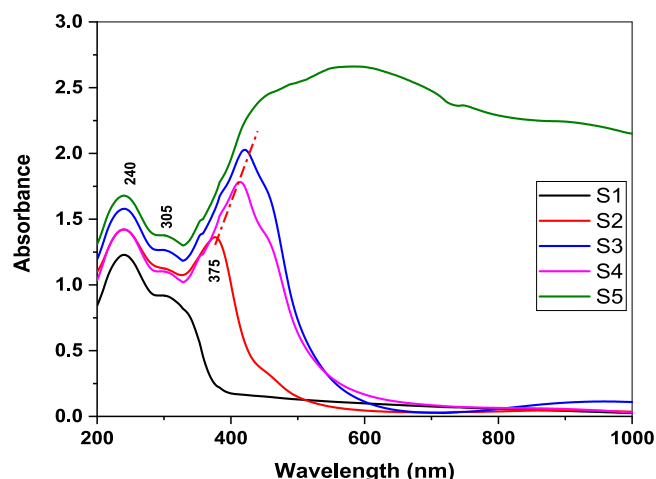


Fig. 4. UV/Vis. Optical Spectral data of studied glasses.

facilitate easy excitation of electrons across bands leading to improved conductivity while larger bandgaps are associated with highly insulating glasses (Elesh et al., 2023; Sallam et al., 2023). Tauc's plots (Fig. 5) are usually used to calculate the energy gap following the equations:

$$(\alpha h\nu)^2 = B(h\nu - E_{g_{\text{direct}}}) \text{ For direct allowed transitions.}$$

$$(\alpha h\nu)^{1/2} = B(h\nu - E_{g_{\text{indirect}}}) \text{ For indirect allowed transitions.}$$

Where  $\alpha$  is the Absorption coefficient,  $h$  Planck's constant,  $\nu$  is the frequency of incident light,  $B$  is a constant,  $E_{g_{\text{direct}}}$  is the direct allowed optical bandgap, and  $E_{g_{\text{indirect}}}$  is the Indirect allowed optical bandgap. Tauc plots can be generated by plotting  $(\alpha h\nu)^2$  and  $(\alpha h\nu)^{1/2}$  versus photon energy ( $h\nu$ ) for direct and indirect allowed transitions respectively. The extrapolation of the linear portions near absorption edges to x-axis intercepts can supply both energies as indicated by Fig. 5 and Table 3.

The IR, UV, and calculated N4 and optical energy gap results are evidence of the presence of iron in both former and modifier sites within the glass structure as  $\text{Fe}^{3+}$  ions.

### 3.4. Calculation of physical parameters

Fig. 6 reveals changes in the measured density and calculated molar volume of the studied glass while Table 3 reports a peripheral change in theoretical and experimental densities when iron oxide is incorporated at the expense of boron oxide, the balancing effects on glass structure led to marginal changes in density and molar volume of the borate glass system. This also reflects the variation of both packing density (Pd) and free volume (Vf) shown in Fig. 7.

The theoretical density can be calculated using the Additive Method assuming that the density of the glass is the weighted sum of the densities of its constituent oxides. The theoretical density ( $\rho_{\text{th}}$ ) can be calculated using the following equation:

$$\rho_{\text{th}} = \sum_{i=0}^n x_i \rho_i$$

Where  $x_i$  is the mole fraction of the  $i^{\text{th}}$  oxide component, and  $\rho_i$  is the density of that oxide.

The observed behavior can be interpreted as (Abou Hussein and Barakat, 2022; Abou Hussein and Abdel-Galil, 2023):

- $\text{Fe}^{3+}$  can act as both a glass network former and a modifier in a borate glass structure. As  $\text{B}_2\text{O}_3$  (glass former) is replaced by  $\text{Fe}_2\text{O}_3$ ,  $\text{Fe}^{3+}$  ions maintain the integrity of the borate glass network, preventing major density fluctuations.
- The boron coordination state in the borate glass network is constrained to be predominantly trigonal  $\text{BO}_3$  units. As more  $\text{Fe}_2\text{O}_3$  is

added, the  $\text{Fe}^{3+}$  ions preferentially occupy interstitial sites without heavily disturbing the boron coordination state.

- Conversion of the  $\text{BO}_3$  function group to  $\text{BO}_4$  unit with the addition of  $\text{Fe}_2\text{O}_3$  combined with the change in density may be balanced with replacing  $\text{B}_2\text{O}_3$  (atomic mass densities  $2.46 \text{ g/cm}^3$ ) with  $\text{Fe}_2\text{O}_3$  (atomic mass densities  $5.25 \text{ g/cm}^3$ ) which does not significantly alter the overall glass density and molar volume as observed by Sallam et al (Sallam et al., 2023).
- Only a small fraction of  $\text{B}_2\text{O}_3$  (typically  $< 10 \text{ mol}\%$ ) can be substituted by  $\text{Fe}_2\text{O}_3$  before phase separation occurs as indicated by the amorphous nature of glass detected by X-ray diffraction (XRD). So the composition variation is not enough to drastically affect overall density.

Other parameters including Ion concentration (N), Polaron radius ( $r_p$ ), Field strength (F), Molar volume of the boron atoms  $V_b$ , and Average boron-boron distance ( $d_{\text{B-B}}$ ), can be calculated as described previously (Basha et al., 2023; Madshal et al., 2023) and listed in the Table 3.

### 3.5. Radiation shielding characteristics

Borate glasses have emerged as effective radiation shielding materials owing to the high neutron capture cross-section of boron, which facilitates strong interaction with neutron radiation. The high cross-section for neutron absorption which is a measure of the probability of a particular nuclear reaction occurring between a neutron and a nucleus makes boron attractive for specialized shielding applications in nuclear reactors, spent fuel storage, medical devices, etc (Basha et al., 2023; Baykal et al., 2023).

Various theoretical and experimental studies have analyzed the influence of glass composition, the presence of modifiers, dopants, etc. on the gamma-ray attenuation and neutron shielding efficiency in borates (Baykal et al., 2023; Kurtulus et al., 2023; Kilic et al., 2023). Key radiation shielding parameters that are used to quantify the protection ability include mass attenuation coefficient, half-value layer thickness, mean free path, tenth value layer, etc.

The mass attenuation coefficient ( $\mu/\rho$ ) indicates the probability of radiation interaction on a per-unit density basis. For effective shielding, glasses require high  $\mu/\rho$  to maximize attenuation (Kurtulus et al., 2023; Kilic et al., 2023). The half-value layer (HVL) thickness signifies the amount of material needed to reduce the initial radiation intensity by half. Lower HVL allows compact and lightweight shield design without compromising protection levels (Baykal et al., 2023). A similar metric is the tenth value layer (TVL) indicating 90 % attenuation. Through compositional optimization, borates with HVL  $< 1 \text{ mm}$  and TVL  $< 2 \text{ mm}$  are feasible (Ali et al., 2022; Levet, 2023).

The mean free path gives the average distance between two successive interactions and needs to be lowered using dopants with high interaction cross-section (Saleh et al., 2022). The radiation shielding characteristics of the prepared glasses were computed using the PhysX/PSD software.

#### 3.5.1. Mass attenuation coefficient (MAC)

Beer-Lambert rule ( $I = I_0 e^{-\mu x}$ ) can be used to determine the interaction of gamma rays with matter through the linear attenuation coefficient parameter  $\mu$ , where,  $I$  and  $I_0$  are the intensities of gamma rays (incident) and (attenuated).

The mass attenuation coefficient ( $\mu_m$ ) is calculated using the linear attenuation coefficient and density of glass ( $\mu_m = \frac{\mu}{\rho}$ ). Accurate values of ( $\mu_m$ ) are necessary to give fundamental information in various fields, including radiation protection, radiation dosimetry, and nuclear diagnostics.

The mass attenuation coefficient expresses the probability that incident photons and matter of a given mass per unit area will interact

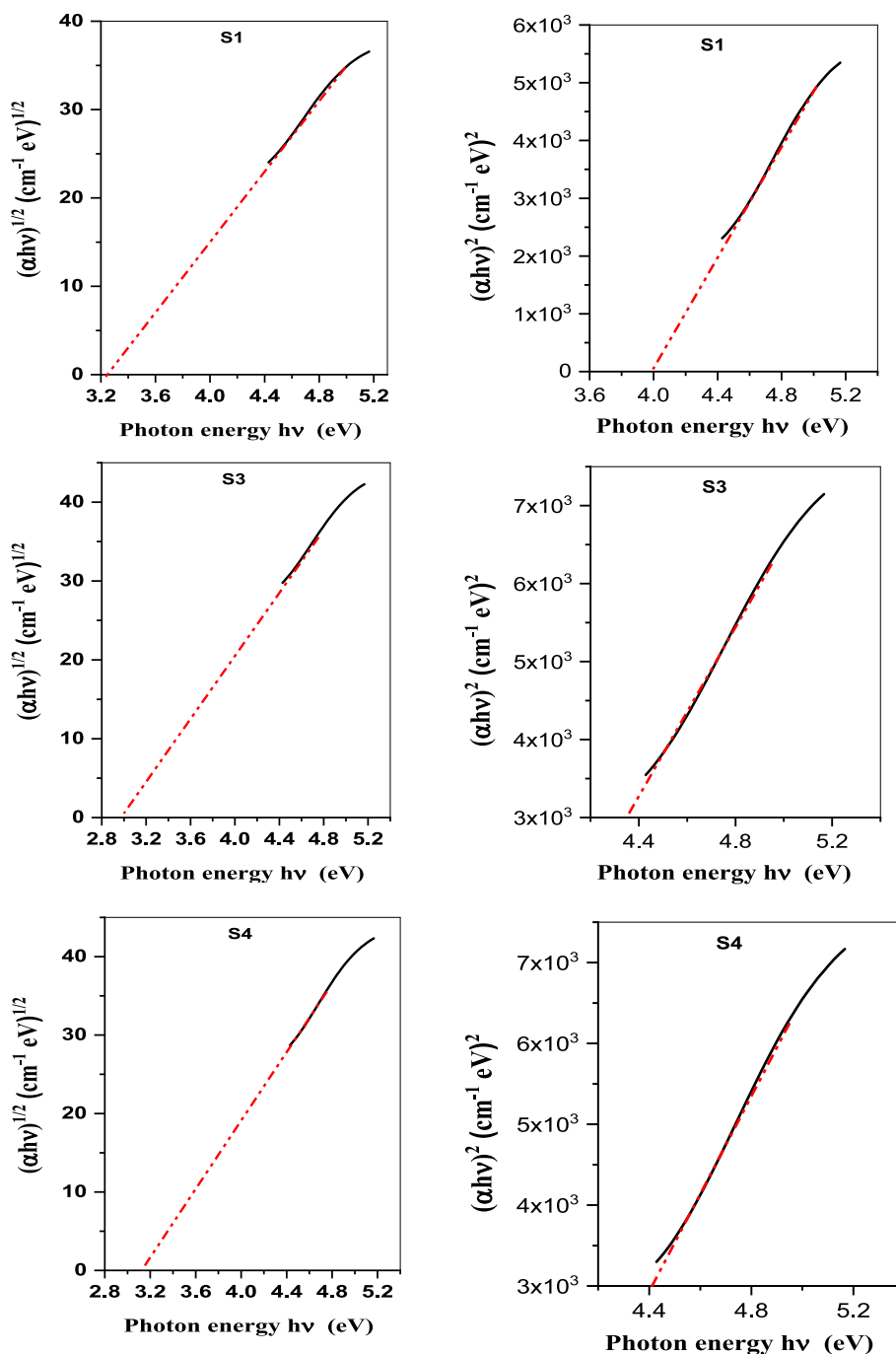


Fig. 5. Tauc's plots of the parent (S1) and selected glass samples (S2, S4) containing iron oxide.

(Saleh et al., 2022). The MAC results plotted against photon energy for all the glasses under study at photon energies ranging from 0.015 to 15 MeV. Fig. 8 shows the relationship between photon energy and  $\text{Fe}_2\text{O}_3$  concentration variations and the MAC for S1-S5 glasses. Because photons interact with matter through different mechanisms depending on their energy, the MAC increases with increasing concentration of Fe and decreases with increasing photon energy. Compton scattering has the advantage that the probability of the photoelectric effect decreases with photon energy (Al-Hadeethi and Tijani, 2019). Moreover, the ratio of  $\mu_m$  is observed to decrease very slowly at high energies, depending on the energy of the incident photon and the  $\text{Fe}_2\text{O}_3$  concentrations.

### 3.5.2. Linear attenuation coefficient (LAC)

The relationship between photon energy and variations in  $\text{Fe}_2\text{O}_3$

concentration and the LAC for S1-S5 studied glasses is depicted in Fig. 9. At low photon energies, the maximum values of  $\mu$  were observed in all the studied glasses. It was revealed that the  $\mu$  values were extremely high in S5 glass and extremely low in S1 glass. This is explained by the glass's chemical makeup. In other words, the  $\mu$  values are raised by the number of components and the atomic numbers of the glass's constituent elements. The highest  $\mu$  values were found for S5 glass because its constituent elements have the largest atomic numbers ( $Z = 5, 11, 20, 15,$  and  $26$  for B, Na, Ca, P, and Fe, respectively) among all the glasses examined.  $\mu$  values decrease above 30 keV, and the cross-section in the considered photon energies is determined by the photoelectric absorption, which varies with the photon the Compton scattering is the cause of the observed decrease (Cheewasukhanont et al., 2022).

**Table 3**  
Experimental, theoretical density, energy gap, and other physical parameters.

Parameters	S1	S2	S3	S4	S5
Density (Experimental) (g/cm <sup>3</sup> ) ± 0.0002	2.63	2.66	2.69	2.74	2.86
Density (Theoretical) (g/cm <sup>3</sup> )	2.66	2.69	2.71	2.77	2.88
E <sub>direct</sub> (eV)	3.23	3.01	3.05	3.16	3.17
E <sub>indirect</sub> (eV)	4.02	4.12	4.33	4.41	4.40
Molar volume(V <sub>m</sub> ) (cm <sup>3</sup> /mol) (±0.0001)	24.98	25.07	25.14	25.28	25.55
Packing density (Pd)	0.628	0.627	0.625	0.623	0.618
Free volume (V <sub>f</sub> ) (cm <sup>3</sup> /mol)	9.285	9.357	9.418	9.535	9.754
Average mol. wt. (MAv)(g)	65.77	66.67	67.57	69.37	72.97
Ion concentration (N) (10 <sup>+20</sup> ions)	–	2.40	4.79	9.52	18.85
Polaron radius (r <sub>p</sub> ) (Å)	–	6.48	5.15	4.09	3.26
Inter-nuclear distance (r <sub>i</sub> ) (Å)	–	16.09	12.78	10.16	8.10
Field strength (F) 10 <sup>+16</sup> (g/molcm <sup>-2</sup> )	–	3.8	6.02	9.52	15
Molar volume of the boron atoms V <sub>b</sub>	21.72	21.42	21.13	20.55	19.51
Average boron–boron distance(d <sub>B-B</sub> )(nm) 10 <sup>+8</sup>	3.30	3.29	3.27	3.24	3.19

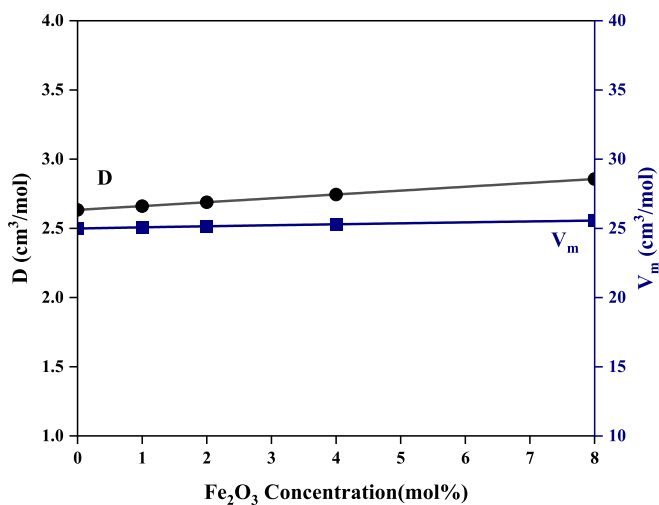


Fig. 6. Variation of density and molar volume with iron oxide addition.

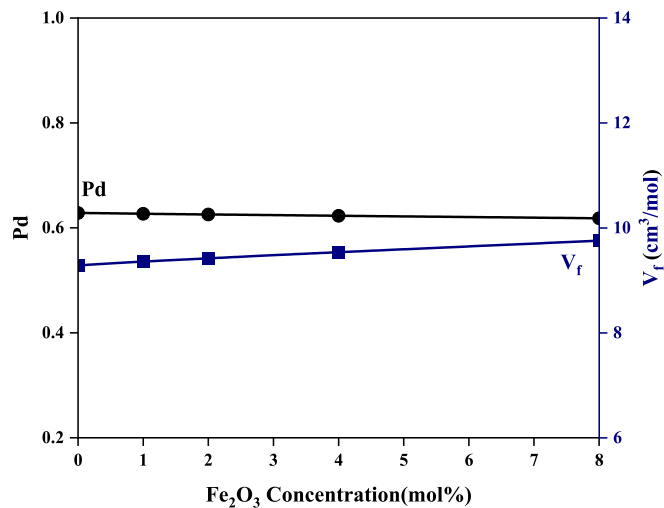


Fig. 7. Variation of packing density and free volume with iron oxide addition.

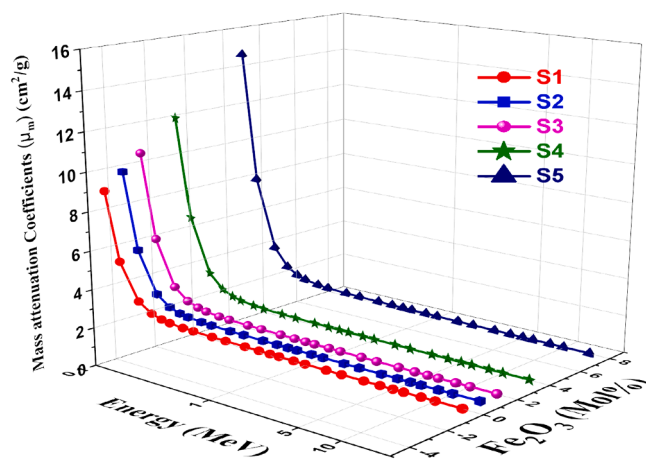


Fig. 8. Variation of MAC vs. photon energy for studied glasses.

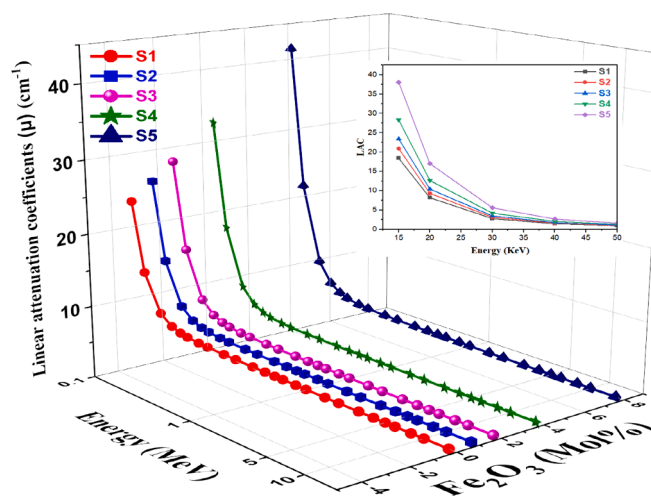


Fig. 9. Variation of LAC vs. photon energy for studied glasses.

3.5.3. Half value layer (HVL), and mean free path (MFP)

HVL is one of the most significant gamma transmission factors in radiation studies and is frequently used to comprehend how various studied glasses interact with gamma rays (Almuqrin et al., 2024; Altowyan et al., 2024; Alomairy et al., 2022). This factor directly indicates the thickness needed to reduce the incident gamma-ray intensity by half. The computed HVL values for the studied glasses under investigation are displayed in Fig. 10. The HVL values increased with photon energy, increased at high photon energies, and decreased with increasing Fe<sub>2</sub>O<sub>3</sub> concentrations, suggesting that the synthesized samples' shielding ability was improved. Another gamma transmission factor, MFP, is depicted in Fig. 11. The distance between a photon's subsequent interactions with glass is known as the MFP (Al-Hadeethi et al., 2020). MFP behaves in a way that is comparable to HVL. In other words, a lot of photons with higher energies can flow through the glass. The MFP value decreases with increasing Fe<sub>2</sub>O<sub>3</sub> content. According to the study, the MFP value for S5 glass is low.

3.5.3.1. Atomic cross-section (ACS) and electronic cross-section (ECS).

The cross-section of each atom shows the intensity of the photon beam during transmission for all processes involving photons and absorber atoms. Figs. 12 and 13, respectively, show atomic cross-section σ<sub>a</sub> and electronic cross-section σ<sub>e</sub>. σ<sub>a</sub> increases at low energy regions due to an increase in Fe<sub>2</sub>O<sub>3</sub> content and then decreases with increasing photon energy. This is explained by the fact that coherent scattering causes σ<sub>a</sub> to

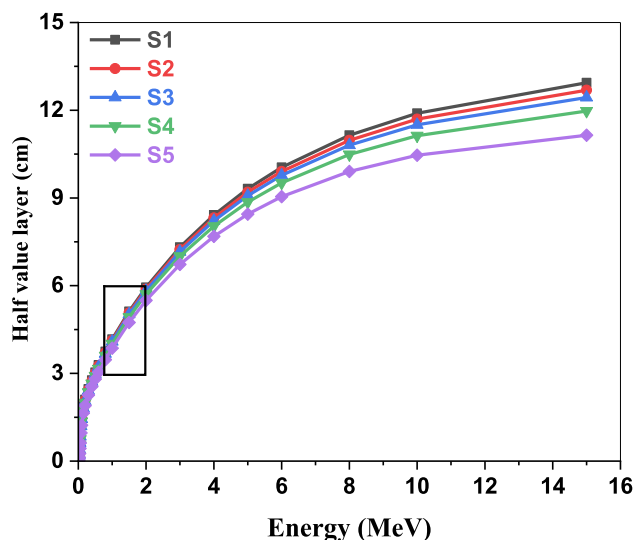


Fig. 10. Variation of HVL with photon energy for the studied glasses.

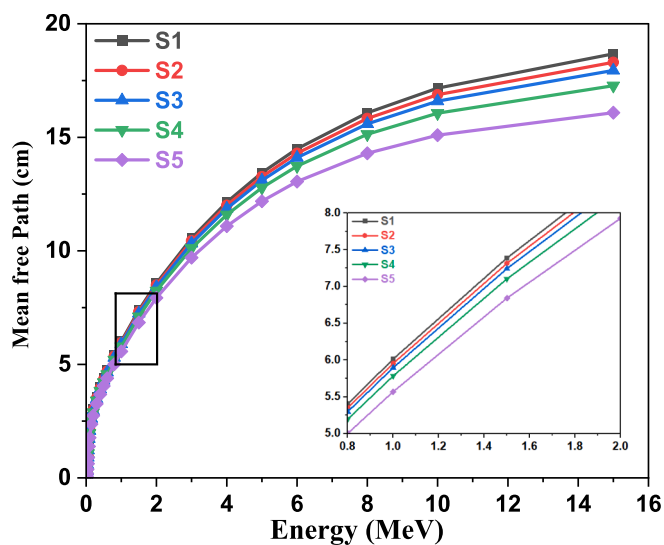


Fig. 11. Variation of MFP with photon energy for the studied glasses.

be sensitive to interference effects at very low energies. As energy increases,  $\sigma_e$  decreases for all studied glass samples (Jiang et al., 2018). As a result, the photon energy utilized, and the chemical makeup of the material determine the values of  $\sigma_a$  (Prajapati et al., 2019).

**3.5.3.2. Effective conductivity  $C_{eff}$  – effective electron density  $N_{eff}$  – and effective atomic number  $Z_{eff}$ .** The variation in effective conductivity ( $C_{eff}$ ) for each sample of glass is shown in Fig. 14. A photon becomes a free electron when it strikes an electron on glass. Also, a variation in the quantity of free electrons would result in an alteration in the electrical conductivity of the substance (Abdelghany et al., 2022). The effective number of electrons per mole is directly proportional to the effective conductivity  $C_{eff}$  of a shielding material for attenuation.  $C_{eff}$  values decrease quickly as photon energy increases, particularly in the region where photoelectric interactions predominate (ALMisned et al., 2021). This is because  $C_{eff}$  has an inverse relationship with photon energy. Effective electron density ( $N_{eff}$ ), which is the electron number per unit mass in complex materials, is calculated by dividing the MAC values by the ECS values.  $N_{eff}$  cannot be expressed as a single number, as in pure element atoms at different photon energies. Fig. 15 shows the  $N_{eff}$  values decrease with increasing energy, but they rise with increasing  $Fe_2O_3$ . As

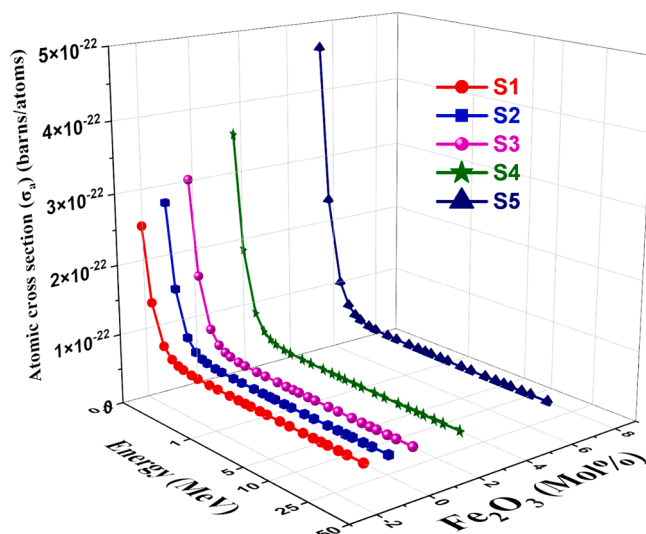


Fig. 12. Variation of  $\sigma_a$  and  $\sigma_{es}$ , respectively vs. photon energy for studied glasses.

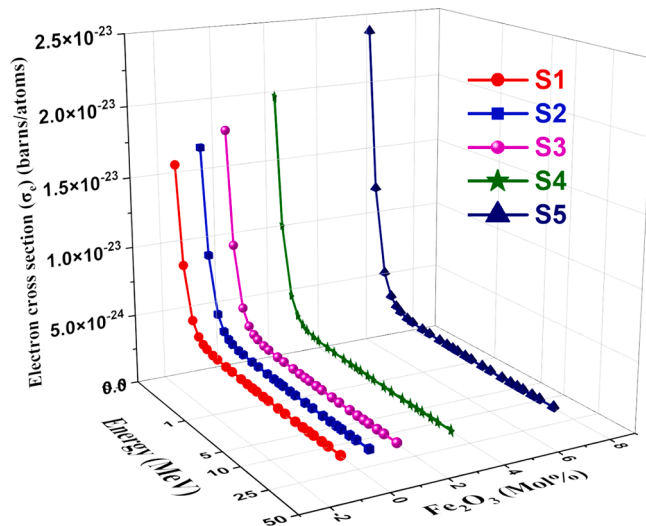
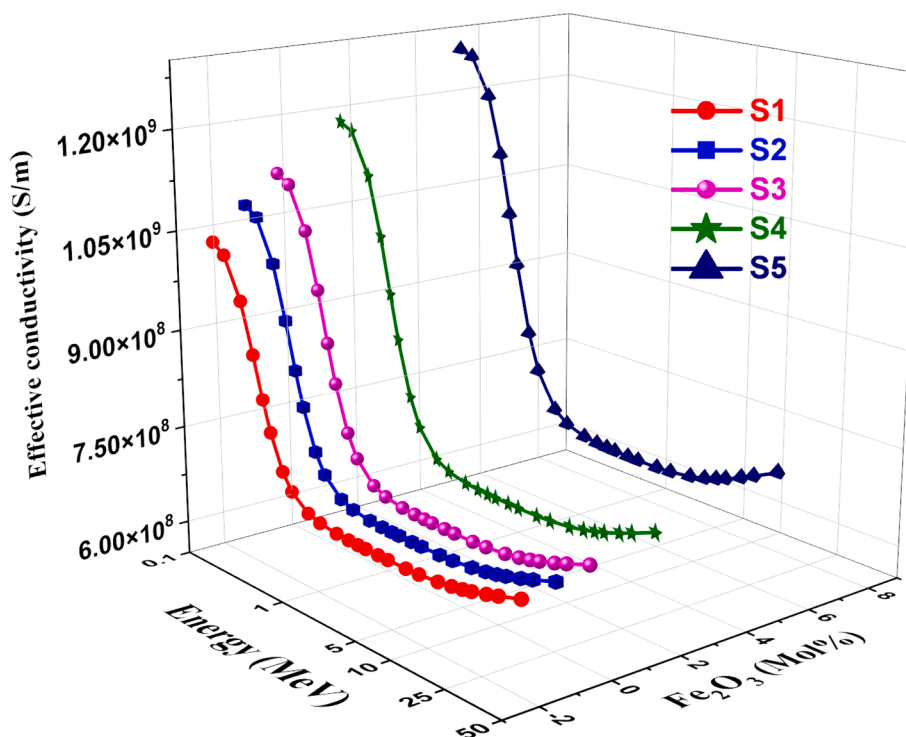
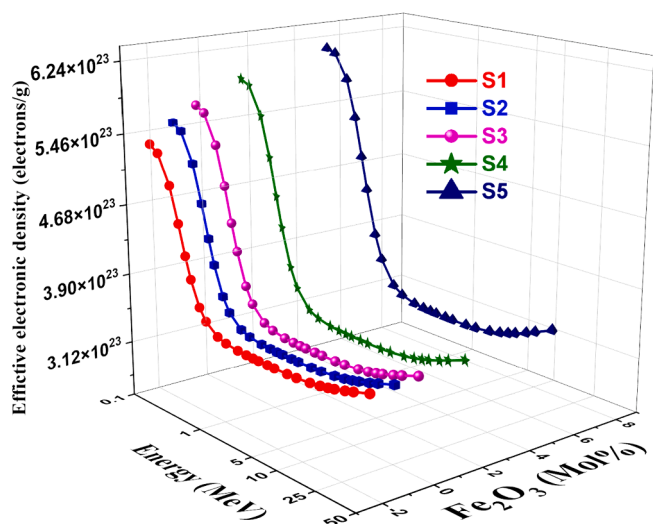
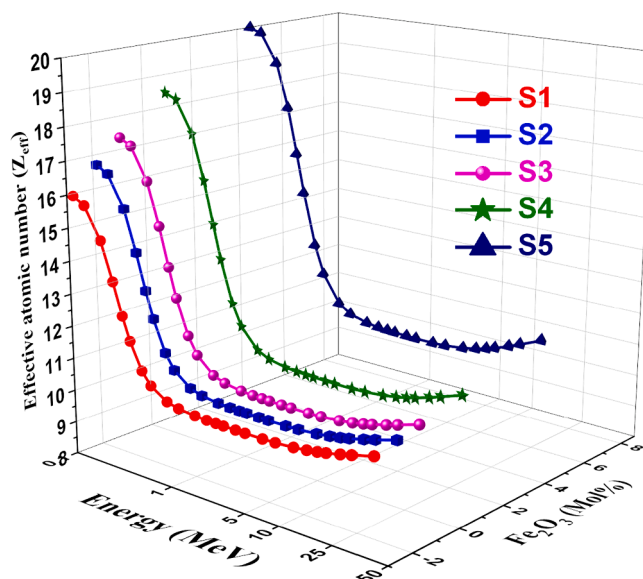


Fig. 13. Variation of  $\sigma_a$  and  $\sigma_{es}$ , respectively vs. photon energy for studied glasses.

shown in Fig. 16, the effective atomic number  $Z_{eff}$  was computed using the glass samples' atomic and electric cross sections. At low energy, the glass samples'  $Z_{eff}$  values tend toward higher values. The photoelectric process causes all manufactured glass samples'  $Z_{eff}$  to rapidly decrease to increase incident energy at low gamma-ray energy. Generally, The effective electron density is related to the polarizability and refractive index of the glass. Higher electron density generally leads to higher refractive indices. The variation of effective electron density with composition can be used to design glasses with desired refractive indices for optical applications like lenses, prisms, and fiber optics. Understanding the effective conductivity is important for designing glasses with specific electrical properties, such as high ionic conductivity for solid-state batteries or low electronic conductivity for insulating materials. Moreover, by calculating the effective atomic number of glasses, researchers and engineers can better understand and optimize the radiation interaction properties of these materials, enabling their effective use in various applications ranging from radiation shielding and dosimetry to X-ray and gamma-ray spectroscopy. These relationships are valuable for tailoring glass properties by modifying the composition or processing conditions, as well as for developing new glass compositions

Fig. 14.  $C_{\text{eff}}$  vs. photon energy for studied glasses.Fig. 15.  $N_{\text{eff}}$  vs. photon energy for studied glasses.Fig. 16.  $Z_{\text{eff}}$  vs. photon energy for studied glasses.

with desired characteristics (Rotkovich et al., 2024; Waida and Rilwan, 2024; Alasali et al., 2024).

**3.5.3.3. Exposure buildup factor (EBF) – And energy absorption buildup factor (EABF).** In general, three regions can be distinguished by three distinct incidents in the interactions between the material and energy: the low-energy photoelectric effect, the intermediate-energy region's Compton scattering, and the high-energy pair production. EBF and EABF are the lowest in the low-energy region because of the photoelectric effect process. Due to the Compton scattering effect, the EBF and EABF rise with increasing energies in the more mid-energy region (Abuzaid et al., 2020). Figs. 17 and 18 display the photon energy dependent EBF and EABF, respectively change for the studied glass at 1–40 MFP. The probability of photons interacting with the material in the range of

15–40 MFP varied with  $Z^2$  after 1 MeV (Kavaz et al., 2020; Ahmed et al., 2024; Rotkovich et al., 2023). As the  $\text{Fe}_2\text{O}_3$  content increased, the EBF and EABF values decreased as well had were affected by the studied glass's chemical composition, and the S5 sample had the lowest EBF and EABF values.

### 3.6. Correlation between low energy and high energy shielding

While most radiation shielding studies focus on high-energy gamma rays or neutrons, there is a growing need to explore shielding materials for low-energy radiation in the UV and visible ranges. This is particularly relevant for applications such as protective coatings, specialized optics,

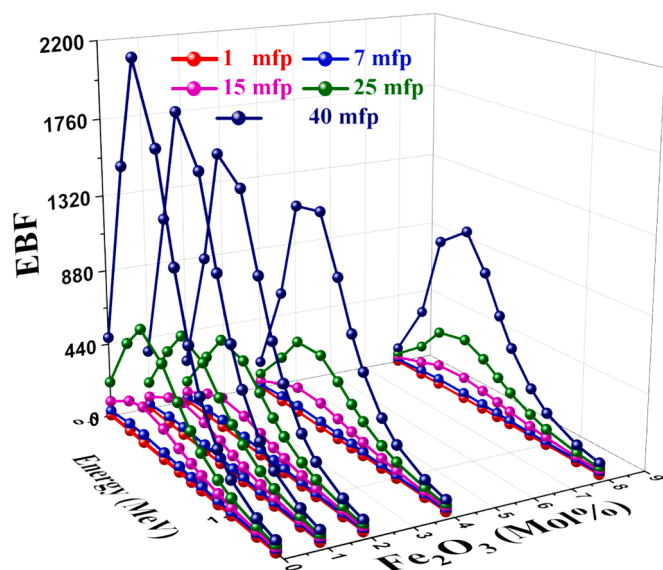


Fig. 17. EBF vs. photon energy for studied glasses.

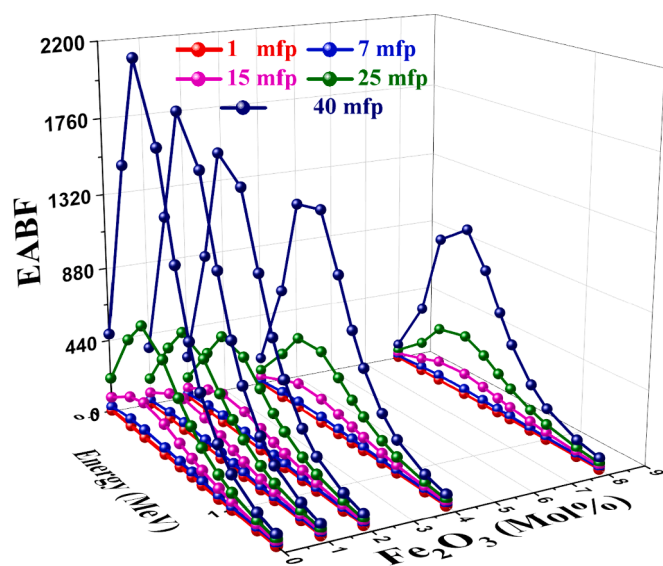


Fig. 18. EABF vs. photon energy for studied glasses.

and shielding in certain instrumentation or sensing devices. The iron-doped soda-lime borophosphate glasses investigated in this study present an opportunity to evaluate their shielding capabilities across a broader energy range, including the UV and visible regions. In addition to the high-energy radiation shielding properties, the attenuation behavior of the iron-doped glasses in the UV and visible range was observed from UV-Vis. Optical absorbance Fig. 4 where the absorbance increases with increasing iron content followed by a decrease in transmittance within the region extended between 200–800 nm. However, the glasses with lower iron oxide concentrations (e.g., 1–4 mol%) exhibit reasonable transmittance in the visible range, making them potential candidates for applications requiring a balance between optical transparency and low-energy radiation shielding.

#### 4. Conclusions

The comprehensive study on iron-doped soda lime borophosphate glasses in the system  $x\text{Fe}_2\text{O}_3-(42.5-x)\text{B}_2\text{O}_3-26\text{CaO}-28.7\text{Na}_2\text{O}-2.8\text{P}_2\text{O}_5$  (x up to 8 mol%) yielded significant insights into their structural

modifications, optical behavior, and remarkable radiation shielding capabilities. X-ray diffraction confirmed their amorphous nature, while FTIR analysis revealed the presence of structural units like  $\text{BO}_3$ ,  $\text{BO}_4$ ,  $\text{PO}_4$ ,  $\text{FeO}_4$ , and  $\text{FeO}_6$  incorporated into the glass network upon iron oxide addition. Particularly, the calculation of the  $N_4$  value, representing the fraction of tetrahedral  $\text{BO}_4$  units, decreased from around 0.5 for the base glass to 0.44 when the iron oxide content reached 8 mol%, suggesting that iron acts as both a network former and modifier. UV-Vis spectra exhibited characteristic absorption bands related to  $\text{Fe}^{3+}$  ions occupying tetrahedral sites, confirming their successful integration into the glass structure. Optical bandgap calculations revealed values ranging from 3.67 eV (direct) and 3.42 eV (indirect) for the base glass to 3.37 eV (direct) and 3.14 eV (indirect) for the 8 mol% iron oxide glass, indicating their suitability for visible light transmission and potential for tailoring electrical conductivity. Evaluation of radiation shielding parameters demonstrated a significant enhancement with increasing iron oxide content due to the high atomic number and density of iron. The mass attenuation coefficient (MAC) values were highest at  $0.548 \text{ cm}^2/\text{g}$  for the 8 mol% iron oxide glass at 0.015 MeV photon energy, compared to  $0.306 \text{ cm}^2/\text{g}$  for the base glass. Furthermore, the half-value layer (HVL), a critical parameter indicating the thickness required to reduce radiation intensity by half, was lowest at 0.56 cm for the 8 mol% iron oxide glass at 0.015 MeV, in contrast to 1.01 cm for the base glass. The effective atomic number ( $Z_{\text{eff}}$ ), a measure of radiation interaction probability, reached a maximum of 26.3 for the 8 mol% iron oxide glass at low energies, compared to 18.5 for the base glass. Additionally, the exposure buildup factor (EBF), which quantifies the buildup of radiation intensity within the shielding material, was minimized to 1.28 for the 8 mol% iron oxide glass at 0.015 MeV and 40 mean free paths. Furthermore, the iron-doped soda-lime borophosphate glasses demonstrated promising shielding capabilities in the low-energy UV and visible ranges, in addition to their high-energy radiation shielding properties. This versatility expands their potential applications to areas such as protective coatings, specialized optics, and shielding in instrumentation or sensing devices where both optical transparency and low-energy radiation shielding are desirable.

#### Consent to participate

All authors participated directly in the current research work.

#### Consent to publish

The authors agree to publish the article under the Creative Commons Attribution License.

#### CRediT authorship contribution statement

**Kholood Alkhamis:** Writing – original draft, Visualization, Formal analysis, Data curation. **Hawra A. Alhasham:** Writing – original draft, Visualization, Methodology. **Albandary Almahri:** Writing – review & editing, Software, Resources, Investigation. **Hussain Alesha:** Writing – original draft, Methodology, Investigation, Formal analysis. **Oumr Adnan Osra:** Writing – review & editing, Software, Formal analysis, Data curation. **S.A. Al-Ghamdi:** Formal analysis, Methodology, Software, Writing – original draft, Writing – review & editing. **Adel M. Binyaseen:** Writing – original draft, Visualization, Methodology, Formal analysis. **Nashwa M. El-Metwaly:** Writing – review & editing, Supervision, Project administration.

#### Declaration of competing interest

The authors declare that they have no known competing financial interests or personal relationships that could have appeared to influence the work reported in this paper.

#### References

- Abdelghany, A.M., 2010. The elusory role of low level doping transition metals in lead silicate glasses. *Silicon* 2, 179–184.

- Abdelghany, A.M., Ouis, M.A., Azooz, M.A., ElBatal, H.A., El-Bassyouni, G.T., 2016. Role of SrO on the bioactivity behavior of some ternary borate glasses and their glass ceramic derivatives. *Spectrochim. Acta A Mol. Biomol. Spectrosc.* 152, 126–133.
- Abdelghany, A.M., ElBatal, H.A., Ramadan, R.M., 2017. The effect of Li<sub>2</sub>O and LiF on structural properties of cobalt doped borate glasses. *J. King Saud Univ.-Sci.* 29 (4), 510–516.
- Abdelghany, A.M., Diab, H.M., Madbouly, A.M., Ezz-ElDin, F.M., 2022. Inspection of radiation shielding proficiency and effect of gamma-ray on ESR and thermal characteristics of copper oxide modified borate bioglasses. *J. Inorg. Organomet. Polym. Mater.* 32 (8), 3204–3219.
- Abdelghany, A.M., El-Batal, H.A., EzzEl-Din, F.M., ElAlialy, N., Okasha, A., Atta, D., Awad, W., 2024. Structural and gamma-ray attenuation of mixed former lead-free borophosphate glasses. *Radiat. Phys. Chem.* 214, 111276.
- Abou Hussein, E.M., Abdel-Galil, A., 2023. Synthesis, optical, chemical and electrical characterizations of  $\gamma$ -irradiated transition metal ions reinforced borate glasses. *J. Non Cryst. Solids* 610, 122302.
- Abou Hussein, E.M., Barakat, M.A., 2022. Structural, physical and ultrasonic studies on bismuth borate glasses modified with Fe<sub>2</sub>O<sub>3</sub> as promising radiation shielding materials. *Mater. Chem. Phys.* 290, 126606.
- Abou Hussein, E.M., Madbouly, A.M., Eldin, F.E., ElAlailly, N.A., 2021. Evaluation of physical and radiation shielding properties of Bi<sub>2</sub>O<sub>3</sub>–B<sub>2</sub>O<sub>3</sub> glass doped transition metals ions. *Mater. Chem. Phys.* 261, 124212.
- Abuzaid, M.M., Susoy, G., Issa, S.A.M., Elshami, W., Kilicoglu, O., Tekin, H.O., 2020. Relationship between melting-conditions and gamma shielding performance of fluoro-sulfo-phosphate (FPS) glass systems: a comparative investigation. *Ceram. Int.*
- Ahmed, E.K., Mahran, H.M., Alrashdi, M.F., Elsafi, M., 2024. Studying the shielding ability of different cement mortars against gamma ray sources using waste iron and BaO microparticles. *Nexus of Future Materials* 1, 1–5.
- Alasali, H.J., Rilwan, U., Mahmoud, K.A., Hanafy, T.A., Sayyed, M.I., 2024. Comparative Analysis of TiO<sub>2</sub>, Fe<sub>2</sub>O<sub>3</sub>. CaO and CuO in borate based glasses for gamma ray shielding. *Nuclear Engineering and Technology.*
- Al-Baradi, A.M., Alotaibi, B.M., Alharbi, N., El-Rehim, A.A., Shaaban, K.S., 2022. Gamma radiation shielding and mechanical studies on highly dense lithium iron borosilicate glasses modified by zinc oxide. *SILICON* 14 (16), 10391–10399.
- Al-Hadeethi, Y., Sayyed, M.I., Al-Buriah, M.S., 2020. Bioactive glasses doped with TiO<sub>2</sub> and their potential use in radiation shielding applications. *Ceram. Int.*
- Al-Hadeethi, Y., Tijani, S.A., 2019. The use of lead-free transparent 50BaO-(50-x) borosilicate-xBi<sub>2</sub>O<sub>3</sub> glass system as radiation shields in nuclear medicine. *J. Alloy. Comp.* 803, 625–630.
- Ali, M.S., Abdelmonem, A.M., Elshamdy, S.K., Shoraiet, G.M., Mustafa, T.M., Hassan, G. S., 2022. The Investigation of Lead Borate Glass Composites for Boron Neutron Capture Therapy Shielding. *Atom Indonesia* 48 (3), 237–246.
- ALMIsned, G., Tekin, H. O., Bilal, G., Ene, A., Kilic, G., Issa, S. A., ... Zakaly, H. M., 2021. Trivalent ions and their impacts on effective conductivity at 300 K and radio-protective behaviors of bismo-borate glasses: a comparative investigation for Al, Y, Nd, Sm, Eu. *Materials*, 14(19), 5894.
- Almuqrin, A.H., Rashad, M., More, C.V., Sayyed, M.I., Elsafi, M., 2024. An experimental and theoretical study to evaluate Al<sub>2</sub>O<sub>3</sub>-PbO-B<sub>2</sub>O<sub>3</sub>-SiO<sub>2</sub>-BaO radiation shielding properties. *Radiat. Phys. Chem.* 111824.
- Alomairy, S., Alrowaili, Z.A., Kebaili, I., Wahab, E.A., Mutuwong, C., Al-Buriah, M.S., Shaaban, K.S., 2022. Synthesis of Pb<sub>3</sub>O<sub>4</sub>-SiO<sub>2</sub>-ZnO-WO<sub>3</sub> glasses and their fundamental properties for gamma shielding applications. *SILICON* 14 (10), 5661–5671.
- Altowyan, A.S., Sayyed, M.I., Kumar, A., Rashad, M., 2024. SrO–ZnO–PbO–B<sub>2</sub>O<sub>3</sub> glassy insights: Unveiling the structural and optical features for gamma ray shielding efficacy. *Opt. Mater.* 152, 115534.
- Basha, B., Alsuifany, S.J., Olarinoye, I.O., Alrowaili, Z.A., Sadeq, M.S., Misbah, M.H., Al-Buriah, M.S., 2023. Synthesis, physical, optical, and radiation attenuation efficiency of Bi<sub>2</sub>O<sub>3</sub>+ SrF<sub>2</sub>+ Li<sub>2</sub>O glass system. *J. Radiat. Res. Appl. Sci.* 16 (4), 100676.
- Baykal, D.S., Kilic, G.Ö.K.H.A.N., Ilik, E., Kavaz, E., ALMIsned, G., Cakirli, R. B., & Tekin, H. O., 2023. Designing a Lead-free and high-density glass for radiation facilities: Synthesis, physical, optical, structural, and experimental gamma-ray transmission properties of newly designed barium-borosilicate glass sample. *J. Alloy. Compd.* 965, 171392.
- Brauer, D.S., Möncke, D., 2016. Introduction to the structure of silicate, phosphate and borate glasses. *Bioactive Glasses* 61–88.
- Brow, R.K., 2000. The structure of simple phosphate glasses. *J. Non Cryst. Solids* 263, 1–28.
- Carta, D., Qiu, D., Guerry, P., Ahmed, I., Abou Neel, E.A., Knowles, J.C., Newport, R.J., 2008. The effect of composition on the structure of sodium borophosphate glasses. *J. Non Cryst. Solids* 354 (31), 3671–3677.
- Cheewasukhanont, W., Siengsanoh, K., Limkitjaroenporn, P., Chaiphaksa, W., Kothan, S., Intachai, N., Kaewkhao, J., 2022. The properties of silicate glass specimens for photon, neutron, and charged particles shielding: The roles of Bi<sub>2</sub>O<sub>3</sub>. *Radiat. Phys. Chem.* 201, 110385.
- Donald, S.B., Swink, A.M., Schreiber, H.D., 2006. High-iron ferric glass. *J. Non Cryst. Solids* 352 (6–7), 539–543.
- Dunaeva, E.S., Uspenskaya, I.A., Pokholok, K.V., Minin, V.V., Efimov, N.N., Ugolkova, E. A., Brunet, E., 2012. Coordination and RedOx ratio of iron in sodium-silicate glasses. *J. Non Cryst. Solids* 358 (23), 3089–3095.
- Dyar, M.D., 1985. A review of Mössbauer data on inorganic glasses: the effects of composition on iron valency and coordination. *Am. Mineral.* 70 (3–4), 304–316.
- Ehrt, D., & Möncke, D. (2002). Charge transfer absorption of Fe<sup>3+</sup> and Fe<sup>2+</sup> complexes and UV radiation induced defects in different glasses. *6th ESG.*
- Elbasuoni, E.G., Abdelghany, A.M., Moustafa, Y.M., El-Damrawi, G., 2024. Borate speciation and structural studies of vanadium ion doping in borate bioglass. *Appl. Phys. A* 130 (2), 1–9.
- Elesh, E., Abul-Nasr, K.T., Abdelghany, A.M., El-Damhogi, D.G., 2023. Thermal annealing enhanced morphological, nonlinear characteristic, and optical features of Victoria blue nanofilms for photonic application. *Optik* 295, 171486.
- Freundenberger, P.T., 2023. *Phosphate and Borophosphate Glasses for Optical and Biomedical Applications* (Doctoral dissertation. Missouri University of Science and Technology).
- Gautam, C., Yadav, A.K., Singh, A.K., 2012, 2012. A review on infrared spectroscopy of borate glasses with effects of different additives. *ISRN Ceram.* 1–17.
- Griscom, D.L., 1978. Borate glass structure. In: *Borate Glasses: Structure, Properties, Applications.* Springer, US, Boston, MA, pp. 11–138.
- Heuser, L., Nofz, M., Müller, R., 2022. Alkali and alkaline earth zinc and lead borate glasses: Sintering and crystallization. *Journal of Non-Crystalline Solids: X* 15, 100116.
- Heuser, L., Nofz, M., 2022. Alkali and alkaline earth zinc and lead borate glasses: Structure and properties. *Journal of Non-Crystalline Solids: X* 15, 100109.
- Jiang, J., Pi, J., Cai, J., 2018. The advancing of zinc oxide nanoparticles for biomedical applications. *Bioinorg. Chem. Appl.* 1–18. Article ID 1062562.
- Kamitsos, E.I., 2003. Infrared studies of borate glasses. *Phys. Chem. Glasses* 44 (2), 79–87.
- Kamitsos, E.I., 2015. Infrared spectroscopy of glasses. *Modern Glass Characterization* 1–42.
- Kavaz, E., El Agawany, F. I., Tekin, H. O., Perişanoğlu, U., & Rammah, Y. S., 2020. Nuclear radiation shielding using barium borosilicate glass ceramics. *J. Phys. Chem. Solid* 142, 109437.
- Khattari, Z.Y., Zakaly, H.M., Alrowaily, A.W., Ene, A., Shams, M.S., Issa, S.A., Rammah, Y.S., 2024. A comprehensive study on optical, physical, mechanical and radiation shielding properties of calcium bismuth borophosphate glass-ceramics with distinct V<sub>2</sub>O<sub>5</sub> contents. *Opt. Quant. Electron.* 56 (1), 10.
- Kilic, G.Ö.K.H.A.N., Ilik, E.R.K.A.N., Kavaz, E., ALMIsned, G., Baykal, D. S., & Tekin, H. O., 2023. Mechanical, gamma rays and neutron radiation transmission properties for some ZnO–TeO<sub>2</sub>–P<sub>2</sub>O<sub>5</sub>–ZnX glasses. *Ceram. Int.* 49 (19), 31773–31783.
- Kim, N.J., Im, S.H., Kim, D.H., Yoon, D.K., Ryu, B.K., 2010. Structure and properties of borophosphate glasses. *Electron. Mater.* 39, 103–106.
- Kurtulus, R., Kavaz, T., Kavaz, E., ALMIsned, G., & Tekin, H. O., 2023. Synthesis, optical, structural, physical, and experimental gamma-ray transmission properties of high-density lead-boro-tellurite glasses: a multi-phases investigation towards providing a behavioral symmetry through lead (II) oxide. *Ceram. Int.* 49 (14), 23189–23196.
- Lepry, W.C., Nazhat, S.N., 2020. The anomaly in bioactive sol-gel borate glasses. *Materials Advances* 1 (5), 1371–1381.
- Levet, A., 2023. Investigation of radiation shielding parameters of boron compounds. *Radiat. Eff. Defects Solids* 1–16.
- Madshal, M.A., Abdelghany, A.M., Behairy, A., El-Damrawi, G., 2023. Shielding parameters and UV spectral studies on modified borate glasses doped with Gd<sub>2</sub>O<sub>3</sub>. *Appl. Phys. A* 129 (11), 759.
- Mansouri, E., Mesbahi, A., Malekzadeh, R., Mansouri, A., 2020. Shielding characteristics of nanocomposites for protection against X-and gamma rays in medical applications: effect of particle size, photon energy and nano-particle concentration. *Radiat. Environ. Biophys.* 59, 583–600.
- Marzouk, M.A., Abo-Naf, S.M., Zayed, H.A., Hassan, N.S., 2017. Glass former effects on photoluminescence and optical properties of some heavy metal oxide glasses doped with transition metal ions. *J. Appl. Spectrosc.* 84, 162–169.
- Marzouk, S.Y., Elbatal, F.H., 2014. Infrared and UV-visible spectroscopic studies of gamma-irradiated Sb<sub>2</sub>O<sub>3</sub>–B<sub>2</sub>O<sub>3</sub> glasses. *J. Mol. Struct.* 1063, 328–335.
- Ohtori, N., Takase, K., Akiyama, I., Suzuki, Y., Handa, K., Sakai, I., Umesaki, N., 2001. Short-range structure of alkaline-earth borate glasses by pulsed neutron diffraction and molecular dynamics simulation. *J. Non Cryst. Solids* 293, 136–145.
- Osipova, L.M., Osipov, A.A., Osipov, A.A., 2019. The Structure of Binary and Iron-Containing ZnO–B<sub>2</sub>O<sub>3</sub> Glass by IR, Raman, and Mössbauer Spectroscopy. *Glas. Phys. Chem.* 45, 182–190.
- Prajapati, S., Singh, B., Kumar, S., Singh, B.K., Shanker, R., 2019. Experimental evidence of molecular coherence effects in the bremsstrahlung radiation processes. *J. Phys. B Atomic Mol. Phys.* 52, 145201.
- Romero-Perez, M., Rincón, J.M., Oliver, C.J.G., D'Ovidio, C., Esparza, D., 2001. Magnetic properties of glasses with high iron oxide content. *Mater. Res. Bull.* 36 (7–8), 1513–1520.
- Rotkovich, A.A., Tishkevich, D.I., Bondaruk, A.A., German, S.A., Razanau, I.U., Zubar, T. I., Trukhanov, A.V., 2023. Epoxy-w composite materials: microstructure, structure, and radiation efficiency. *Adv Phys Res* 5 (3), 133–145.
- Rotkovich, A.A., Tishkevich, D.I., German, S.A., Bondaruk, A.A., Dashkevich, E.S., Trukhanov, A.V., 2024. A study of the morphological, structural, and shielding properties of epoxy-W composite. *Nexus of Future Materials* 1, 13–19.
- Sadeq, M.S., Abdo, M.A., 2021. Effect of iron oxide on the structural and optical properties of alumino-borate glasses. *Ceram. Int.* 47 (2), 2043–2049.
- Saleh, E.E., Algradee, M.A., Alreshedi, F., Al-Fakeh, M.S., El-Fiki, S.A., Youssef, G.M., El Sharbini, T.M., 2022. Synthesis and nuclear radiation shielding ability of Li<sub>2</sub>O-ZnO-P<sub>2</sub>O<sub>5</sub> glasses: The role of Yb<sub>2</sub>O<sub>3</sub>. *J. Electron. Mater.* 51 (12), 7283–7296.
- Sallam, O.I., Ezz-ElDin, F.M., Elalaily, N.A., 2023. Spectroscopic studies on the reducing effect of  $\gamma$ -irradiation on borosilicate glass modified by Dy<sub>2</sub>O<sub>3</sub>. *J. Mol. Struct.* 1285, 135473.
- Shashikala, H.D., Udayashankar, N.K., 2020. Influence of Fe<sup>3+</sup> and Mn<sup>2+</sup> Ions on Structural, Thermal, Optical and Mechanical Properties of Mixed Alkali Zinc Borate Glass System. National Institute of Technology Karnataka, Surathkal). Doctoral dissertation.

- Topper, B., Möncke, D., Youngman, R.E., Valvi, C., Kamitsos, E.I., Varsamis, C.P., 2023. Zinc borate glasses: properties, structure and modelling of the composition-dependence of borate speciation. *PCCP* 25 (8), 5967–5988.
- Volotinen, T.T., Pehlivan, I.B., 2022. Optical studies of mutual redox and partitioning of coordination sites between  $Ce^{3+}/Ce^{4+}$  and  $Fe^{2+}/Fe^{3+}$  ions in  $Na_2O-CaO-SiO_2$  glass. *J. Non Cryst. Solids* 593, 121749.
- Waida, J., Rilwan, U., 2024. A Comparative Analysis of Radon-222 Concentration in Water Sources and its Potential Stomach and Lungs Doses: A Case Study of Borno State University Campus and its Environs. *Nexus of Future Materials* 1, 39–50.
- Yiannopoulos, Y.D., Chryssikos, G.D., Kamitsos, E.I., 2001. Structure and properties of alkaline earth borate glasses. *Phys. Chem. Glasses* 42 (3), 164–172.
- Youssef, N.H., Belkhiria, M.S., Videau, J.J., Amara, M.B., 2000. Investigation of the physico-chemical properties of calcium borophosphate glasses. Effect of the substitution of sodium for calcium. *Mater. Lett.* 44 (5), 269–274.